Time-Resolved VUV ARPES at 10.8 eV photon energy and MHz repetition rate

Simone Peli,[1] Denny Puntel,[2] Damir Kopic,[1] Benjamin Sockol,[3] Fulvio Parmigiani,[1,4] and Federico Cilento[1,*]

[1] *Elettra - Sincrotrone Trieste S.C.p.A., Strada Statale 14, km 163.5, Trieste, Italy*
[2] *Dipartimento di Fisica, Università degli Studi di Trieste, 34127 Trieste, Italy*
[3] *Department of Physics, Massachusetts Institute of Technology, Cambridge, MA 02139, USA*
[4] *International Faculty, University of Cologne, Albertus-Magnus-Platz, 50923 Cologne, Germany*

The quest for mapping the femtosecond dynamics of the electronic band structure of complex materials over their full first Brillouin zone is pushing the development of schemes to efficiently generate ultrashort photon pulses in the VUV energy range. At present, the critical aspect in Time- and Angle-Resolved Photoelectron Spectroscopy (TR-ARPES) is to combine a high photon energy with high photoemission count rates and a narrow pulse-bandwidth, necessary to achieve high energy resolution, while preserving a good time resolution and mitigating space-charge effects. Here we describe a novel approach to produce light pulses at 10.8 eV, combining high repetition rate operation (1-4 MHz), high energy resolution ($\sim$ 26 meV) and space-charge free operation, with a time-resolution of $\sim$700 fs. These results have been achieved by generating the ninth harmonic of a Yb fiber laser, through a phase-matched process of third harmonic generation in Xenon of the laser third harmonic. The full up-conversion process is driven by a seed pulse energy as low as 10 μJ, hence is easily scalable to multi-MHz operation. This source opens the way to TR-ARPES experiments for the investigation of the electron dynamics over the full first Brillouin zone of most complex materials, with unprecedented energy and momentum resolutions and high count rates. The performances of the setup are tested by TR-ARPES on the topological insulator Bi_2Se_3.

I. INTRODUCTION

Angle-Resolved Photoelectron Spectroscopy (ARPES) has gained a prominent role for its ability to measure simultaneously the binding energy and the momentum of the electrons in a solid [1–3], allowing to directly visualize the electronic band structure. In ARPES experiments, the binding energy E_B and the parallel momentum $\hbar k_{\parallel}$ of the electrons are easily determined by the energy and momentum conservation laws of the photoemission process, once the electron's kinetic energy E and emission angle θ are measured by an electron analyzer:

$$E = h\nu - W - E_B \tag{1}$$

$$\hbar k_{\parallel} = \sqrt{2m_e E} \cdot \sin\theta \tag{2}$$

$h\nu$ is the incident photon energy, W is the material's work function. Eq.1 and Eq.2 show that the accessible ranges of E_B and $\hbar k_{\parallel}$ are both set by the photon energy, which then plays a key role.

The use of synchrotron light sources to measure the photoelectron dynamics in the extreme ultraviolet (EUV) has been recently reported, however this approach prevents the study of the sub-picosecond electron dynamics [4]. In the last years, the advent of Free Electron Lasers (FELs) opened to the possibility to access the femtosecond photoelectron dynamics [5], at the expense of a lower signal statistics and space charge. Pioneering TR-PES experiments on complex materials have been reported [6], also with the use of modern momentum-microscope energy analyzers, optimizing the percentage of collected photoelectrons [7]. In addition, the space charge issue can be rationalized by detailed modelling of the photoelectron cloud, in order to restore quantitative information [8]. A different route to TR-ARPES, that overcomes these limits, is based on the use of table-top laser sources, and in the last years, a number of laser-ARPES endstations have been developed [9–12]. Indeed, the use of laser light pulses of high peak-power allows to take advantage of non-linear optical effects in crystals and gases to generate ultra-violet (UV) photon energies suitable for ARPES experiments and it is naturally apt to perform ultrafast time-resolved measurements.

In table-top laser-based ARPES setups the UV and vacuum-ultraviolet (VUV) pulses are commonly generated with two methods. Frequency up-conversion in non-centrosymmetric crystals is the most used and efficient method to produce low harmonics (typically the 4^{th} or 5^{th}). Nowadays, the novel KBBF crystal can push the limit of frequency conversion up to 7.56 eV [12, 13]. With this photon energy, and considering a take-off angle of 45°, the maximum crystal momentum achievable is 0.64 Å^{-1}, hence smaller than the extension of the first Brillouin zone of most materials. This limitation is overcome by the High Harmonic Generation (HHG) process, which exploits the ionization and the subsequent recombination of the electrons in a noble gas by means of high intensity visible pulses [14, 15]. Since the recombination probability is of the order of 10^{-6}, a reasonable photon flux is achieved only with seed pulses of hundreds of μJ energy. Nowadays, this limits the operational repetition rate (r.r.) to $<$ 200 kHz [16].

Here, we follow a different approach and develop a compact source for TR-ARPES experiments, that overcomes both the low photon energy attainable by non-linear-crystals and the low throughput of HHG based systems. A cascade of non-linear wave-mixing stages ex-

* federico.cilento@elettra.eu

ploiting the second-order (in crystals) and third-order (in gas) non-linear susceptibilities brings to VUV pulses of 10.8 eV photon energy, with tunable r.r. up to 4 MHz. The key process exploited here is the third harmonic generation (THG) in Xenon, as further discussed later. In the panorama of VUV radiation generation in Xenon for ARPES experiments [17–20], the present time-resolved VUV setup ranks in the first place in terms of throughput, photon energy, energy resolution, stability and reliability, while keeping a reasonable time resolution. After describing the experimental setup, we present the measurements performed on the topological insulator Bi_2Se_3 in order to test the setup performances.

II. EXPERIMENTAL SETUP

A. Generation of 10.8 eV light

Pulses at 10.8 eV results from three stages of frequency up-conversion, occurring in solids or gases behaving as non-linear media after the interaction with high intensity electric fields. In general, the polarization P of the medium has a non-linear response to the electric field E:

$$P(t) = \epsilon_0(\chi^{(1)}E(t) + \chi^{(2)}E^2(t) + \chi^{(3)}E^3(t) + \dots) \quad (3)$$

where $\chi^{(n)}$ is the n-th order susceptibility of the medium and ϵ_0 the vacuum permittivity. Since gases are isotropic and centrosymmetric [21], their second order susceptibility vanishes and the first non-linear term is $\chi^{(3)}$, responsible for third harmonic generation (THG). The phase matching condition for frequency up-conversion in gases takes advantage from the anomalous dispersion found in the vicinity of the allowed dipole transitions. In particular, anomalous dispersion in Xenon occurs in the spectral region 113.5 nm (10.92 eV) to 117 nm (10.59 eV) [22, 23]. When the third harmonic falls in this range, *i.e.* the driving wavelength is in the 340.5–351 nm range, efficient phase matched THG can occur [24]. Hence, the third harmonic at 345 nm of a Yb-based laser with output at 1035 nm can be used as a seed for its ninth harmonic (115 nm) in a perfect phase-matching condition, achieving an efficiency of 10^{-4}–10^{-5} [19]. On the contrary, Ti:Sapphire lasers at 800 nm are not suitable for efficient THG in Xenon, since frequency tripling of a 400 nm seed happens as a six-wave mixing because of the positive dispersion of Xenon in this range [25].

B. Experimental Layout

The fundamental light for harmonic generation is provided by a Yb fiber-based laser (Coherent Monaco 1035) producing 290 fs pulses at 1035 nm and 40 μJ energy/pulse, at a base r.r. of 1 MHz, hence with 40 W average power.

Following the scheme of Figure 1, the fundamental beam at ω_1 is frequency-doubled in a 2.5 mm thick type-I BBO crystal (with $\theta = 23.3°$), producing photons at 517 nm (2.39 eV) with a maximum efficiency of 50%. The beams at ω_1 and ω_2 interact collinearly in a type-II BBO crystal (1.7 mm thick and $\theta = 32.3°$) to generate the third harmonic ω_3 at 345 nm (3.59 eV) via a sum-frequency-generation (SFG) process, with a maximum efficiency of 20%. A type-II interaction is convenient since the ≈300 fs pulse duration requires no delay compensation. The third harmonic is isolated by wavelength separators reflecting ω_3. The THG beam is focused by a f=+100 mm focal length lens in a small gas cell (ambience A) filled with Xenon where, through a four-wave mixing THG process, the ninth harmonic ω_9 at 115 nm (10.78 eV) is generated. The gas cell and the refocusing chamber (ambience B) are isolated by a LiF wedged window (with $\sim$ 20% transmittivity at 115 nm) with a 5° apex angle. This window also acts as a prism, separating the beams at ω_3 and ω_9. The refocusing chamber is purged with a constant flux of nitrogen [26]. After separation, the VUV beam is reflected from a spherical mirror (with a 250 mm radius of curvature), that refocuses the beam on the sample. A motorized plane mirror drives the beam inside the ARPES chamber (ambience C). Both spherical and plane mirrors have a coating optimized for 120 nm. The UHV TR-ARPES chamber and the refocusing chamber are divided by a LiF viewport. The VUV light hits the sample at an incidence angle of $\theta = 30°$ with respect to normal emission. The electron analyzer is a SPECS Phoibos 225, and samples are mounted on a six degrees-of-freedom cryo-manipulator. The pump beam is obtained by a polarizing beamsplitter plate and passes through a delay stage for pump-probe experiments; it is focused on the sample by a 150 cm focal length lens. Thanks to a $\lambda/2$ waveplate, the ratio between the pump and probe beam powers can be set arbitrarily depending on the experimental requirements. In order to determine the VUV probe spot size, we make use of a YAG scintillator placed at the sample position. With a CMOS camera, we acquire the VUV-beam induced fluorescence, that we analyze in order to extract an average Full-Width at-Half-Maximum (FWHM) for the beam. The 1035 nm pump beam spot size has been determined in a similar way, but directly using the copper sample holder as a target. The FWHM values we obtained are (260±20) μm and (350±20) μm, for the probe and the pump, respectively. The spatial overlap is obtained by overlapping the pump spot on the probe spot fluorescence on the YAG screen, which is positioned exactly in the sample plane after the equilibrium photoemission has been optimized. The temporal overlap is obtained directly from the time-resolved photoemission signal. The setup, owing to its compact design, showed to be optically and mechanically stable over days of use. The pump-probe spatial overlap is usually checked and eventually optimized every time a new sample is introduced. An aging problem affects the LiF wedged window, resulting in a reduction of the VUV flux that is restored after cleaning and eventually replacing the optical element.

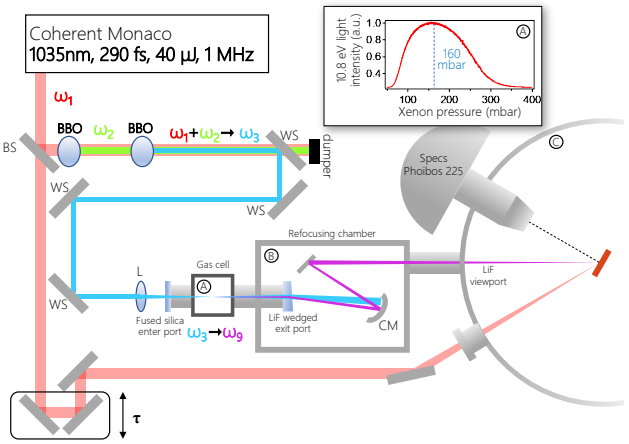

FIG. 1. **Layout of the experimental setup.** BBO: β-BaB_2O_4; BS: beam splitter; WS: wavelength separator; L: lens; CM: curved mirror; ambience A: gas cell; ambience B: refocusing chamber; ambience C: ARPES chamber. The inset shows the 10.8 eV light intensity as a function of the Xenon pressure in the gas cell.

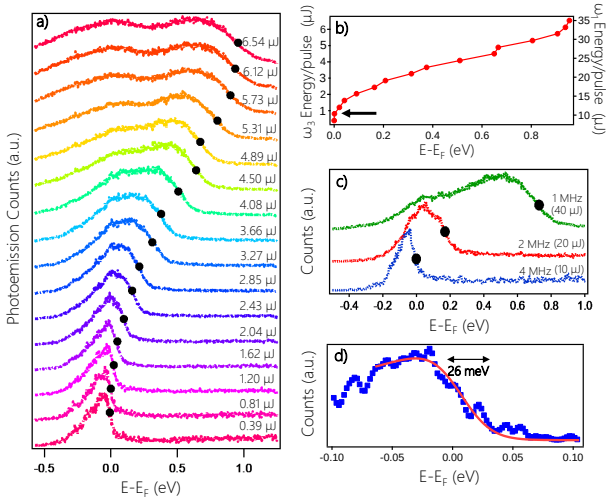

FIG. 2. **Space charge effect.** (**a**) EDCs extracted from photoemission maps from polycrystalline gold. The curves are normalized and shifted for clarity. The black dots indicate the Fermi edge position. The values of E_F are reported in panel (**b**) as a function of the ω_3 (left axis) and ω_1 (right axis) energy per pulse. (**c**) Space charge effect versus repetition rate. (**d**) Blue curve of panel (**c**) with superimposed the fit to the data, revealing a $\simeq$26 meV energy resolution.

III. PHOTOEMISSION AT 10.8 EV

The THG phase-matching conditions in the tight focusing regime are optimized by tuning the Xenon pressure, measured with a piezo pressure gauge, in the gas cell (A). The 10.8 eV light intensity is recorded using a channeltron electron multiplier, while slowly varying the gas pressure. The resulting pressure tuning curve is shown in the inset of Figure 1; the maximum is found at $\approx$160 mbar.

One of the major problems of photoemission by pulsed laser sources is space charge. The use of intense femtosecond laser pulses causes a large number of electrons being simultaneously emitted in a small volume. Electrons in a crowded cloud experience strong Coulomb repulsions leading to a distortion of the spatial distribution of the outcoming electrons [27]. We evaluated the space charge using a polycrystalline gold sample. Energy distribution curves (EDCs) integrated over 10° emission are reported in Figure 2(a). We show the raw data, which are affected by a non-uniform detector responsivity. The acquisition time varied from 10 s at the highest flux to 60 s at the lowest flux. The top curve, taken at 1 MHz, shows a huge distortion of the Fermi edge, shifted by $\sim$1 eV from the target position ($E - E_F = 0$) when the 345 nm beam is kept at an energy/pulse of 6.54 μJ. Exploiting an attenuator integrated in the source, we investigate the shift of the Fermi edge as a function of the energy/pulse at 345 nm, as reported in Figure 2(a) (the curves have been normalized and offset for clarity). The position of the Fermi energy (black dots) has been extracted from a fit of a Fermi-Dirac distribution multiplied by a Lorentzian, convoluted with a Gaussian accounting for the experimental resolution, and reported in panel (b) of Figure 2 as a function of the third harmonic energy/pulse (left axis) and the corresponding fundamental energy/pulse (right axis). From the graph we can identify a region below $\sim$0.81 μJ/pulse (10% of the third harmonic maximum power, highlighted by the black arrow) in which the spectra are space-charge–free. The count rate at 1 MHz assures fast acquisition times also in this space-charge-free regime. In this condition, only $\sim$25% (10.56 μJ/pulse) of the total laser power is required for VUV light generation, leaving a $\sim$75% available for the pump beam, opening to the possibility of seeding an Optical Parametric Amplifier (OPA) for tuning the pump photon energy. Taking advantage of the extensive r.r. tunability offered by the laser system, and having found that just $\sim$10 μJ/pulse at 1035 nm suffices for 115 nm generation, we investigate the possibility to mitigate space-charge by simply increasing the r.r. and working at full laser power. In this way, the total flux can be even larger. In Figure 2(c), we report the EDCs acquired at maximum laser output power and setting the r.r. to 1 MHz (40 μJ/pulse), 2 MHz (20 μJ/pulse) and 4 MHz (10 μJ/pulse). As expected, at 4 MHz the space charge effect completely vanishes. This fact demonstrates the effectiveness of the approach, beneficial for laser ARPES measurements at equilibrium. From the fit of the EDC curve measured at 4 MHz, we estimate an overall energy resolution of $\simeq$26 meV (zoomed energy range of $\pm$100 meV in Figure 2(d)), including the analyzer and experimental contributions. We estimate this value to be in excess of the 115 nm beam bandwidth, thus leaving room for further improvement.

IV. TR-ARPES ON Bi_2Se_3

We performed TR-ARPES measurements on bismuth-selenide (Bi_2Se_3), which has been widely studied and proposed as a candidate for spintronics and quantum computing applications [28]. Like other topological insulators [29], this material is characterized by an energy gap between the occupied and unoccupied states in the bulk band structure and by a gapless topological surface state (TSS) at the surface [30–32]. In Bi_2Se_3 crystals, the impurities due to Se vacancies lead to a net n-doping of the material with a consequent partial population of the bulk conduction band (BCB) crossing the Fermi energy. The Bi_2Se_3 electronic band structure is sketched in Figure 3(e).

The study of the relaxation dynamics was carried out at $k_y = 0$, that identifies the $\overline{\Gamma}$-$\overline{\mathrm{M}}$ high symmetry direction. As a pump we used the fundamental beam with 30 μJ/cm^2 fluence, that produces no detectable space charge. Both pump and probe beams were set to p-polarization through $\lambda/2$ wave-plates. The r.r. was set to 1 MHz, in order to control the sample average heating by the pump pulse, and 10 μJ/pulse were used for the probe. Figure 3(a) shows the ARPES spectrum at equilibrium, before the pump excitation. All the features of Bi_2Se_3 down to 500 meV below E_F are clearly recognized, with the linear dispersion of the TSS and the Dirac point at ∼400 meV below E_F. The diffused intensity inside the Dirac cone is due to the population of the bottom of the BCB, having its minimum at $E_B = 200$ meV. All around the BCB there is an intense and narrow rim. This is recognized as the spectral fingerprint of a two-dimensional electron gas (EG) confined at the surface [33], originating from extrinsic defects and impurities, due to the sample aging [34]. In panels (b),(c) and (d) we show the same spectra 1 ps, 2 ps and 3 ps after the pump excitation, respectively. For a more direct visualization of the pump-induced effect, we show in panels (f), (g) and (h) the difference between the excited spectra and the spectrum collected at negative delay. The high momentum resolution permits to distinguish clearly the contributions from each of the three bands. Maps in panels (a)–(d) are the result of 10 min acquisition time.

In TR-ARPES studies on Bi_2Se_3 the focus has been primarily on the TSS and the CB features [35–38]. However, information on the dynamics of the two-dimensional electron gas is still lacking. In Figures 3(i) and (j) we report the photoemission intensity variation ΔI as a function of pump-probe delay t, extracted from the regions indicated by coloured circles in panel (f). The full dynamics has been recorded in about 1 hour. We investigated the relaxation dynamics of the three different bands 70 meV above (shades of purple) and below (shades of yellow) the Fermi level. We superimposed the three curves (after intensity renormalization) and show that no differences are evident. Since our time resolution exceeds the timescale of the fastest interband scattering process (∼ 200 fs), the scattering of the electrons between the surface states and the bulk conduction band [38] cannot be resolved. At longer delays, instead, the cooling mechanism is mainly due to intraband scattering, thus being very similar for the three different bands [36].

We used this measurement to estimate the overall time resolution. We extracted the relaxation dynamics of the electronic population integrating over the area enclosed in the green rectangle in Figure 3(f) at $E - E_F \simeq 0.22$ eV above the Fermi level and we reported the relaxation curve in Figure 3(k). The fit function is the convolution of a Gaussian function, accounting for the experimental resolution, and a single exponential decay. The fitting procedure returned a decay time τ=1.57 ps and an overall time resolution of ∼700 fs. This value is larger than the minimum attainable temporal resolution, set by the pump-probe cross-correlation (XC), that in our setup would be equal to ≈420 fs. The value we measure is larger than the XC because of the elongation of the VUV probe pulse, as a consequence of the wavefront tilt acquired during the pulse propagation through the wedged window used as a wavelength separator. This effect can be avoided by replacing the wedged window with a time-preserving grating-based wavelength selector, at the expense of the system compactness. In addition, a much shorter pump pulse (40-50 fs) obtained by a non-collinear Optical Parametric Amplifier (NOPA) could be used, leading to a final time resolution better than 300 fs.

V. DISCUSSION AND CONCLUSIONS

We developed a setup for TR-ARPES at 10.8 eV photon energy, with <26 meV energy resolution, ∼700 fs time resolution and r.r. up to 4 MHz. This approach improves both the momentum mapping capability of conventional crystal-based setups and the low conversion efficiency of HHG systems. Efficient VUV generation by optimal phase-matched THG in the negatively-dispersing region of Xenon (113.5–117 nm) is obtained by using a Yb fiber-based laser producing pulses at 1035 nm. The tunability of the r.r. renders the system highly versatile. High flux measurements at 4 MHz and 10 μJ pulse energy can be performed, where the space-charge is completely mitigated. This configuration can be used especially for equilibrium measurements, since the thermal heating by the pump pulse could affect the sample under scrutiny. Alternatively, lower repetition rates can be used for time-resolved measurements. We proved that at 1 MHz a space charge free condition is achieved using an energy/pulse of only 10 μJ (∼ 25% of the total laser output power), thus leaving the excess power available to seed an OPA for tuning the pump wavelength. In conclusion, we report on a development allowing to measure the out-of-equilibrium photoemission intensity over the full first Brillouin zone of most complex materials (up to 0.9-

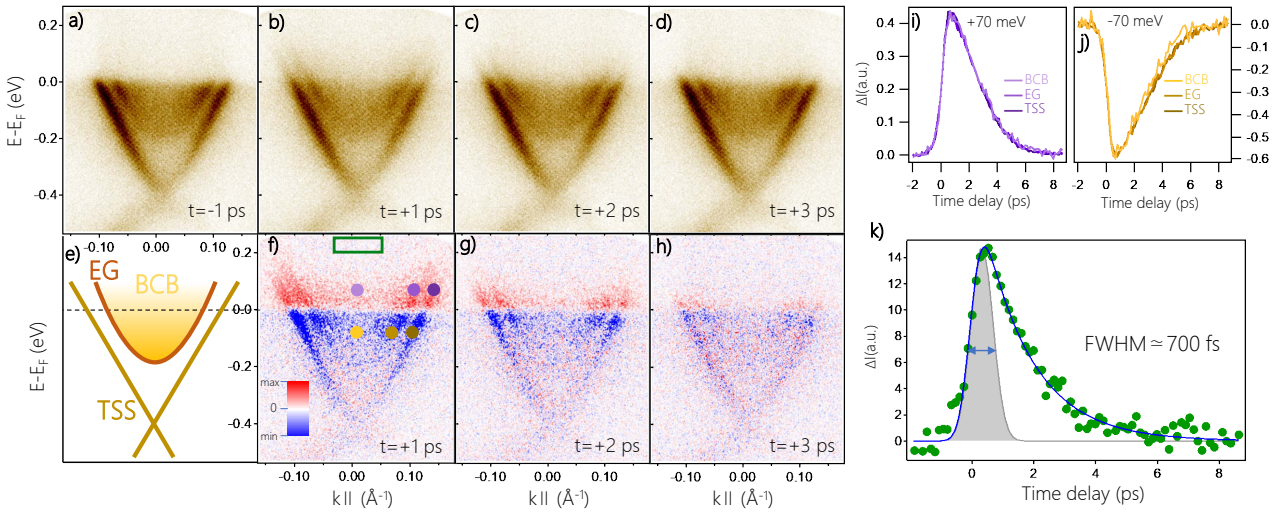

FIG. 3. **Electron dynamics in Bi_2Se_3.** Panels (**a**)-(**d**) show the E vs k_x dispersion at $k_y = 0$ before the arrival of the pump (**a**) and 1 ps, 2 ps, 3 ps (**b**, **c**, **d**) after photo-excitation at 1.2 eV. (**e**) Sketch of the three spectral features as reported in [33] (TSS: Topological Surface State; BCB: Bulk Conduction Band; EG: Electron Gas). The differential maps (**f**-**h**) emphasize the photo-induced effects. The superimposed curves in panels (**i**) and (**j**) show the dynamics integrated on the coloured areas of panel (**f**). (**k** Dynamics integrated in the green rectangle in panel **f** and fitted to extract the time resolution (blue curve, see text).

1 Å^{-1}) with high energy and momentum resolutions, and high count-rates without space charge. We demonstrate the capabilities of the setup by investigating the topological insulator Bi_2Se_3 and reporting high quality ARPES and TR-ARPES maps. Our results demonstrate a compact, stable and inexpensive approach for the generation of high photon energy laser pulses for ARPES, which surpasses the conventional 4th or 5th harmonics generation approaches widely used in the previous decades.

ACKNOWLEDGMENTS

The authors would like to thank Aleksander De Luisa for the design of the refocusing vacuum chamber and W. Bronsch for the careful proofreading of the manuscript.

[1] N. V. Smith and M. M. Traum, Angular dependence of photoemission from the (110) face of gaas, Phys. Rev. Lett. **31**, 1247 (1973).

[2] A. Damascelli, Z. Hussain, and Z.-X. Shen, Angle-resolved photoemission studies of the cuprate superconductors, Rev. Mod. Phys. **75**, 473 (2003).

[3] X. J. Zhou, T. Cuk, T. Devereaux, N. Nagaosa, and Z.-X. Shen, Angle-resolved photoemission spectroscopy on electronic structure and lectron–phonon coupling in cuprate superconductors, in *Handbook of High-Temperature Superconductivity: Theory and Experiment*, edited by J. R. Schrieffer and J. S. Brooks (Springer New York, New York, NY, 2007) pp. 87–144.

[4] R. Costantini, M. Stredansky, D. Cvetko, G. Kladnik, A. Verdini, P. Sigalotti, F. Cilento, F. Salvador, A. D. Luisa], D. Benedetti, L. Floreano, A. Morgante, A. Cossaro, and M. Dell'Angela, Anchor-sundyn: A novel end-station for time resolved spectroscopy at the aloisa beamline, Journal of Electron Spectroscopy and Related Phenomena **229**, 7 (2018).

[5] J. Rossbach, J. R. Schneider, and W. Wurth, 10 years of pioneering x-ray science at the free-electron laser flash at desy, Physics Reports **808**, 1 (2019), 10 years of pioneering X-ray science at the Free-Electron Laser FLASH at DESY.

[6] S. Hellmann, C. Sohrt, M. Beye, T. Rohwer, F. Sorgenfrei, M. Marczynski-Bühlow, M. Kalläne, H. Redlin, F. Hennies, M. Bauer, A. Föhlisch, L. Kipp, W. Wurth, and K. Rossnagel, Time-resolved x-ray photoelectron spectroscopy at FLASH, New Journal of Physics **14**, 013062 (2012).

[7] D. Kutnyakhov, R. P. Xian, M. Dendzik, M. Heber, F. Pressacco, S. Y. Agustsson, L. Wenthaus, H. Meyer, S. Gieschen, G. Mercurio, A. Benz, K. Bühlman, S. Däster, R. Gort, D. Curcio, K. Volckaert, M. Bianchi, C. Sanders, J. A. Miwa, S. Ulstrup, A. Oelsner, C. Tusche, Y.-J. Chen, D. Vasilyev, K. Medjanik, G. Brenner, S. Dziarzhytski, H. Redlin, B. Manschwetus, S. Dong, J. Hauer, L. Rettig, F. Diekmann, K. Rossnagel, J. Demsar, H.-J. Elmers, P. Hofmann, R. Ernstorfer, G. Schönhense, Y. Acremann, and W. Wurth, Time- and momentum-resolved photoemission studies using time-of-flight momentum microscopy at a free-electron laser, Review of Scientific Instruments **91**, 013109 (2020),

https://doi.org/10.1063/1.5118777.

[8] M. Dell'Angela, T. Anniyev, M. Beye, R. Coffee, A. Föhlisch, J. Gladh, S. Kaya, T. Katayama, O. Krupin, A. Nilsson, D. Nordlund, W. F. Schlotter, J. A. Sellberg, F. Sorgenfrei, J. J. Turner, H. Öström, H. Ogasawara, M. Wolf, and W. Wurth, Vacuum space charge effects in sub-picosecond soft x-ray photoemission on a molecular adsorbate layer, Structural Dynamics **2**, 025101 (2015), https://doi.org/10.1063/1.4914892.

[9] J. Faure, J. Mauchain, E. Papalazarou, W. Yan, J. Pinon, M. Marsi, and L. Perfetti, Full characterization and optimization of a femtosecond ultraviolet laser source for time and angle-resolved photoemission on solid surfaces, Review of Scientific Instruments **83**, 043109 (2012), https://doi.org/10.1063/1.3700190.

[10] C. L. Smallwood, C. Jozwiak, W. Zhang, and A. Lanzara, An ultrafast angle-resolved photoemission apparatus for measuring complex materials, Review of Scientific Instruments **83**, 123904 (2012), https://doi.org/10.1063/1.4772070.

[11] Y. Ishida, T. Togashi, K. Yamamoto, M. Tanaka, T. Kiss, T. Otsu, Y. Kobayashi, and S. Shin, Time-resolved photoemission apparatus achieving sub-20-mev energy resolution and high stability, Review of Scientific Instruments **85**, 123904 (2014), https://doi.org/10.1063/1.4903788.

[12] G. L. L. Z. L. Y. Xingjiang Zhou, Shaolong He and W. Zhang, New developments in laser-based photoemission spectroscopy and its scientific applications: a key issues review, Reports on Progress in Physics. Physical Society **81**, 062101 (2018).

[13] G. Liu, G. Wang, Y. Zhu, H. Zhang, G. Zhang, X. Wang, Y. Zhou, W. Zhang, H. Liu, L. Zhao, J. Meng, X. Dong, C. Chen, Z. Xu, and X. J. Zhou, Development of a vacuum ultraviolet laser-based angle-resolved photoemission system with a superhigh energy resolution better than 1mev, Review of Scientific Instruments **79**, 023105 (2008), https://aip.scitation.org/doi/pdf/10.1063/1.2835901.

[14] M. Lewenstein, P. Balcou, M. Y. Ivanov, A. L'Huillier, and P. B. Corkum, Theory of high-harmonic generation by low-frequency laser fields, Phys. Rev. A **49**, 2117 (1994).

[15] S. Mathias, L. Miaja-Avila, M. M. Murnane, H. Kapteyn, M. Aeschlimann, and M. Bauer, Angle-resolved photoemission spectroscopy with a femtosecond high harmonic light source using a two-dimensional imaging electron analyzer, Review of Scientific Instruments **78**, 083105 (2007), https://doi.org/10.1063/1.2773783.

[16] R. Cucini, T. Pincelli, G. Panaccione, D. Kopic, F. Frassetto, P. Miotti, G. M. Pierantozzi, S. Peli, A. Fondacaro, A. De Luisa, A. De Vita, P. Carrara, D. Krizmancic, D. T. Payne, F. Salvador, A. Sterzi, L. Poletto, F. Parmigiani, G. Rossi, and F. Cilento, Coherent narrowband light source for ultrafast photoelectron spectroscopy in the 17–31 ev photon energy range, Structural Dynamics **7**, 014303 (2020), https://doi.org/10.1063/1.5131216.

[17] M. H. Berntsen, O. Götberg, and O. Tjernberg, An experimental setup for high resolution 10.5 ev laser-based angle-resolved photoelectron spectroscopy using a time-of-flight electron analyzer, Review of Scientific Instruments **82**, 095113 (2011), https://doi.org/10.1063/1.3637464.

[18] Y. He, I. M. Vishik, M. Yi, S. Yang, Z. Liu, J. J. Lee, S. Chen, S. N. Rebec, D. Leuenberger, A. Zong, C. M. Jefferson, R. G. Moore, P. S. Kirchmann, A. J. Merriam, and Z.-X. Shen, Invited article: High resolution angle resolved photoemission with tabletop 11 ev laser, Review of Scientific Instruments **87**, 011301 (2016), https://doi.org/10.1063/1.4939759.

[19] Z. Zhao and Y. Kobayashi, Realization of a mw-level 10.7-ev ($\lambda = 115.6$ nm) laser by cascaded third harmonic generation of a yb:fiber cpa laser at 1-mhz, Opt. Express **25**, 13517 (2017).

[20] A. Zong, A. Kogar, Y.-Q. Bie, T. Rohwer, C. Lee, E. Baldini, E. Ergeçen, M. B. Yilmaz, B. Freelon, E. J. Sie, H. Zhou, J. Straquadine, P. Walmsley, P. E. Dolgirev, A. V. Rozhkov, I. R. Fisher, P. Jarillo-Herrero, B. V. Fine, and N. Gedik, Evidence for topological defects in a photoinduced phase transition, Nature Physics **15**, 27 (2019).

[21] J. F. REINTJES, Nonlinear optical parametric processes in liquids and gases (Academic Press, 1984).

[22] R. A. Ganeev and T. Usmanov, Generation of picosecond radiation continuously tunable in the range 113.5–117.0 nm, Quantum Electronics **26**, 903 (1996).

[23] R. A. Ganeev and T. Usmanov, Frequency conversion of picosecond radiation in ultraviolet (338-366 nm) and vacuum ultraviolet (113.5-117.0 nm) ranges, Journal of Optics A: Pure and Applied Optics **2**, 550 (2000).

[24] A. Kung, J. Young, and S. Harris, Generation of 1182-Å radiation in phase-matched mixtures of inert gases, Applied Physics Letters **22**, 301 (1973), https://doi.org/10.1063/1.1654647.

[25] F. Cilento, A. Crepaldi, G. Manzoni, A. Sterzi, M. Zacchigna, P. Bugnon, H. Berger, and F. Parmigiani, Advancing non-equilibrium arpes experiments by a 9.3 ev coherent ultrafast photon source, Journal of Electron Spectroscopy and Related Phenomena **207**, 7 (2016).

[26] Z. Zhao, K. Kuroda, A. Harasawa, T. Kondo, S. Shin, and Y. Kobayashi, Monolithic lif or mgf2 lens-window-prism device for coherent 10.7 ev beam source with 1 mhz repetition rate, Chin. Opt. Lett. **17**, 051406 (2019).

[27] S. Hellmann, K. Rossnagel, M. Marczynski-Bühlow, and L. Kipp, Vacuum space-charge effects in solid-state photoemission, Phys. Rev. B **79**, 035402 (2009).

[28] I. Garate and M. Franz, Inverse spin-galvanic effect in the interface between a topological insulator and a ferromagnet, Phys. Rev. Lett. **104**, 146802 (2010).

[29] H. Zhang, C.-X. Liu, X.-L. Qi, X. Dai, Z. Fang, and S.-C. Zhang, Topological insulators in bi2se3, bi2te3 and sb2te3 with a single dirac cone on the surface, Nature Physics **5**, 438 (2009).

[30] Z.-H. Pan, E. Vescovo, A. V. Fedorov, D. Gardner, Y. S. Lee, S. Chu, G. D. Gu, and T. Valla, Electronic structure of the topological insulator bi_2se_3 using angle-resolved photoemission spectroscopy: Evidence for a nearly full surface spin polarization, Phys. Rev. Lett. **106**, 257004 (2011).

[31] D. Lu, I. M. Vishik, M. Yi, Y. Chen, R. G. Moore, and Z.-X. Shen, Angle-resolved photoemission studies of quantum materials, Annual Review of Condensed Matter Physics **3**, 129 (2012), https://doi.org/10.1146/annurev-conmatphys-020911-125027.

[32] Z.-H. Zhu, G. Levy, B. Ludbrook, C. N. Veenstra, J. A. Rosen, R. Comin, D. Wong, P. Dosanjh, A. Ubaldini, P. Syers, N. P. Butch, J. Paglione, I. S. Elfimov, and A. Damascelli, Rashba spin-splitting control at the surface of the topological insulator bi_2se_3, Phys. Rev. Lett.

107, 186405 (2011).

[33] M. Bianchi, D. Guan, S. Bao, J. Mi, B. B. Iversen, P. D. C. King, and P. Hofmann, Coexistence of the topological state and a two-dimensional electron gas on the surface of bi2se3, Nature Communications **1**, 128 (2010).

[34] C. Chen, S. He, H. Weng, W. Zhang, L. Zhao, H. Liu, X. Jia, D. Mou, S. Liu, J. He, Y. Peng, Y. Feng, Z. Xie, G. Liu, X. Dong, J. Zhang, X. Wang, Q. Peng, Z. Wang, S. Zhang, F. Yang, C. Chen, Z. Xu, X. Dai, Z. Fang, and X. J. Zhou, Robustness of topological order and formation of quantum well states in topological insulators exposed to ambient environment, Proceedings of the National Academy of Sciences **109**, 3694 (2012), https://www.pnas.org/content/109/10/3694.full.pdf.

[35] J. Sobota, S.-L. Yang, D. Leuenberger, A. Kemper, J. Analytis, I. Fisher, P. Kirchmann, T. Devereaux, and Z.-X. Shen, Ultrafast electron dynamics in the topological insulator bi2se3 studied by time-resolved photoemission spectroscopy, Journal of Electron Spectroscopy and Related Phenomena **195**, 249 (2014).

[36] M. Hajlaoui, E. Papalazarou, J. Mauchain, G. Lantz, N. Moisan, D. Boschetto, Z. Jiang, I. Miotkowski, Y. P. Chen, A. Taleb-Ibrahimi, L. Perfetti, and M. Marsi, Ultrafast surface carrier dynamics in the topological insulator bi2te3, Nano Letters **12**, 3532 (2012), pMID: 22658088, https://doi.org/10.1021/nl301035x.

[37] A. Crepaldi, B. Ressel, F. Cilento, M. Zacchigna, C. Grazioli, H. Berger, P. Bugnon, K. Kern, M. Grioni, and F. Parmigiani, Ultrafast photodoping and effective fermi-dirac distribution of the dirac particles in bi_2se_3, Phys. Rev. B **86**, 205133 (2012).

[38] Y. H. Wang, D. Hsieh, E. J. Sie, H. Steinberg, D. R. Gardner, Y. S. Lee, P. Jarillo-Herrero, and N. Gedik, Measurement of intrinsic dirac fermion cooling on the surface of the topological insulator bi_2se_3 using time-resolved and angle-resolved photoemission spectroscopy, Phys. Rev. Lett. **109**, 127401 (2012).